Hindawi
International Journal of RF and Microwave Computer-Aided Engineering
Volume 2023, Article ID 3599970, 9 pages
https://doi.org/10.1155/2023/3599970

Research Article

Broadband Polarization-Decoupled Metasurface for Generating Tailored Dual-Polarization Conical Beams

Lingjun Yang,[1] **Beier Ying**,[2] **and Sheng Sun**[1]

[1]*School of Electronic Science and Engineering, University of Electronic Science and Technology of China, Chengdu, China*
[2]*Glasgow College, University of Electronic Science and Technology of China, Chengdu, China*

Correspondence should be addressed to Sheng Sun; sunsheng@ieee.org

Received 15 February 2023; Accepted 17 August 2023; Published 14 October 2023

Academic Editor: Morteza Shahpari

Conical beam antenna plays a significant role in providing stable access to satellite signals for moving communication terminals. Although metasurfaces have been used to generate conical beams, most of them can only reflect conical beams with identically distributed and mirror-symmetric phase responses for left-hand circular polarization and right-hand circular polarization, which can hinder the dual-polarization applications of metasurfaces. In this study, a metasurface is designed to independently manipulate dual-polarized excitations in broadband. To achieve the broadband control of conical beams, broadband conditions for both geometric and propagation phases are developed. Differently, metasurface designed in this study consists of three types of distinguishingly shaped elements, which can provide more degree of freedom in dual-polarization broadband design. In addition, a design method is developed for metasurface to generate the cone angle tailorable conical beams. Via fabricating a metasurface following the proposed method, the designed metasurface is verified in theorem, simulation, and experiment that it can generate desired conical beams with tailored divergent angles and phase responses covering a bandwidth from 12.5 GHz to 17 GHz.

1. Introduction

In today's communication systems, humans, vehicles, and various moving objects performing unregular movements have become the carriers of satellite-based communication terminals [1–5]. However, this moving characteristic makes it difficult for these terminals to keep relatively still with satellites to have stable access to satellite signals. To maintain a qualified performance between terminal antennas on moving objects and satellites, a circumferential radiation pattern is expected for terminal antennas. Conical beam antenna with its strongest radiation on a conical surface deviating a certain angle from the normal and covering a large area has been proposed to guarantee stable access to satellites for moving objects [4, 5], particularly, the orbital angular momentum (OAM) beam, a kind of conical beam with identical polarization along the conical surface. Unlike vector conical waves with different polarization [6, 7], OAM conical beams can promote stable reception and communication while the receiver moves. Meanwhile, OAM conical beams have been widely used in nanoparticle manipulation [8], superimaging resolution [9], and data communications [10, 11].

For many years, methods have been developed on generating conical beams such as antenna arrays [12, 13], traveling-wave antennas [10, 11], holographic plates [14], elliptical patch antennas [15], and spiral phase plates [16]. However, generating conical beams with these traditional methods usually depends on complex feeding networks and bulky structures. In recent years, metasurfaces composed of elements with artificially engineered two-dimensional structures are applied in electromagnetic wave manipulation [17–19], which shows an advantage in generating and controlling conical beams. For example, metasurfaces based on resonant structure can generate vector conical beams [6, 7] and OAM conical beams [20–23] in a narrow bandwidth. Moreover, metasurfaces satisfying the Pancharatnam-Berry (PB) phase can introduce a frequency-independent abrupt phase, which can benefit broadband fabrication for circularly polarized (CP) beams [24–26]. Nevertheless, PB-phase-only metasurface cannot present independent phase responses for both

left-hand circular polarization (LHCP) and right-hand circular polarization (RHCP) excitations. The propagation phase is introduced into metasurface design to solve this problem. The propagation phase, an additional variable, makes it possible to independently control phase responses for both RHCP and LHCP excitations (so-called polarization-decoupled strategy) [27–35]. Normally, in most published work, only a single type of element was used for propagation phase adjustment, which can provide a limited degree of freedom to achieve the required broadband phase responses. Therefore, different types of elements are proposed in this study. On the other hand, efforts should be put into designing dual-polarization conical beams with tailored divergent angles or OAM mode in broadband.

In this paper, we investigate the relationship between metasurface and generated conical beams aiming at generating tailored conical beams with expected phase responses (OAM modes) or cone angles for LHCP and RHCP incidences via a single metasurface shown in Figure 1(a). Specifically, this work can be categorized into three aspects. Firstly, we propose the constraints of phase responses for broadband polarization-decoupled elements. Secondly, we develop three broadband polarization-decoupled elements displayed in Figure 1(b) to compose a metasurface, which can realize the broadband polarization decoupling. Thirdly, we establish a theory to tailor the generated conical beams over dual polarization. To verify the effectiveness of proposed elements and theories, we fabricate a metasurface that generates cone angle independently tailored OAM conical beams for dual polarization, illustrating a good conformity with desired cone angle and OAM mode for both LHCP and RHCP excitations.

2. Phase Responses for Broadband Polarization-Decoupled Elements

For PB phase reflective elements with a self-centered rotation angle of β, the designed phase responses can be ideally expressed by [36]

$$r_{ll}(\omega) = 0.5\left[\left(r_{xx}(\omega) - r_{yy}(\omega)\right) + j\left(r_{yx}(\omega) + r_{xy}(\omega)\right)\right]e^{-2j\beta}, \tag{1a}$$

$$r_{lr}(\omega) = 0.5\left[\left(r_{xx}(\omega) + r_{yy}(\omega)\right) + j\left(r_{yx}(\omega) - r_{xy}(\omega)\right)\right], \tag{1b}$$

$$r_{rl}(\omega) = 0.5\left[\left(r_{xx}(\omega) + r_{yy}(\omega)\right) - j\left(r_{yx}(\omega) - r_{xy}(\omega)\right)\right], \tag{1c}$$

$$r_{rr}(\omega) = 0.5\left[\left(r_{xx}(\omega) - r_{yy}(\omega)\right) - j\left(r_{yx}(\omega) + r_{xy}(\omega)\right)\right]e^{2j\beta}, \tag{1d}$$

in which β is the orientation angle of a specific element and the two-letter index refers to the polarization states of reflected and incident waves. From (1a)–(1d), a good performance of a reflective polarization-decoupled element can be achieved by suppressing the cross-polarized reflection coefficients into zero, which is achieved by using mirror-symmetric elements and adjusting the magnitude of x and y copolarized reflection coefficients into unity with a 180° phase difference between them ($\phi_{xx} - \phi_{yy} = \pi$). Therefore, the reflection coefficients for LHCP and RHCP can be described as

$$r_{ll} = R_{ll}e^{j\phi_{ll}} = e^{j(\phi_{xx}-2\beta)}, \tag{2a}$$

$$r_{lr} = 0, \tag{2b}$$

$$r_{rl} = 0, \tag{2c}$$

$$r_{rr} = R_{rr}e^{j\phi_{rr}} = e^{j(\phi_{xx}+2\beta)}. \tag{2d}$$

From (2a) and (2d), phase responses of LHCP and RHCP are $\phi_{ll} = \phi_{xx} - 2\beta$ and $\phi_{rr} = \phi_{xx} + 2\beta$. This means that arbitrary phase distributions of ϕ_{ll} and ϕ_{rr} can be independently designed by controlling the propagation phase ϕ_{xx} and the orientation angle or so-called geometric phase β of each element [28].

Here, we aim to analyze the frequency-related phase responses. Based on (2a)–(2d), the geometric phase β and the propagation phase response or termed initial phase α of a element, denoted as ϕ_{xx} in (2a)–(2d), can be described as

$$\beta = \frac{1}{4}[\phi_{rr}(\omega) - \phi_{ll}(\omega)], \tag{3a}$$

$$\alpha(\omega) = \frac{1}{2}[\phi_{rr}(\omega) + \phi_{ll}(\omega)]. \tag{3b}$$

To achieve the broadband control of LHCP and RHCP conical beams, we propose two necessary conditions for both geometric and propagation phases. First, both geometric and propagation phases should cover a 2π range. Second, the phase gradient between neighbored elements should remain the same within desired bandwidth. For geometric phase, the phase coverage can be fulfilled by rotating the orientation angle β of each element indicated by (3a) if the broadband 180° phase difference of x and y copolarized reflection coefficients has been satisfied ($\phi_{xx}(\omega) - \phi_{yy}(\omega) \approx \pi$, or $|r_{ll}| \approx 1$). Additionally, the CP phases of elements related to geometric phase are orientation-related-only and frequency-unrelated as indicated in (3a), which can benefit the broadband design. Regarding to propagation phase design, if N different elements are used to discrete the propagation phase, phase responses of the N elements should satisfy the relationship

$$N \cdot \Delta\alpha = 2\pi, \tag{4a}$$

$$\Delta\alpha = \alpha_i(\omega) - \alpha_{i-1}(\omega), \quad (i \in [1, 2, \cdots, N-1]), \tag{4b}$$

in which α_i is the propagation phase of the ith different element and $\Delta\alpha$ is the phase gradient between neighbored elements.

3. Elements for Broadband Polarization Decoupling

In this study, the phase gradient $\Delta\alpha$ is 60°, so six types of elements are required according to (4a). From (2a) and (2d), elements satisfying PB phase conditions have the same

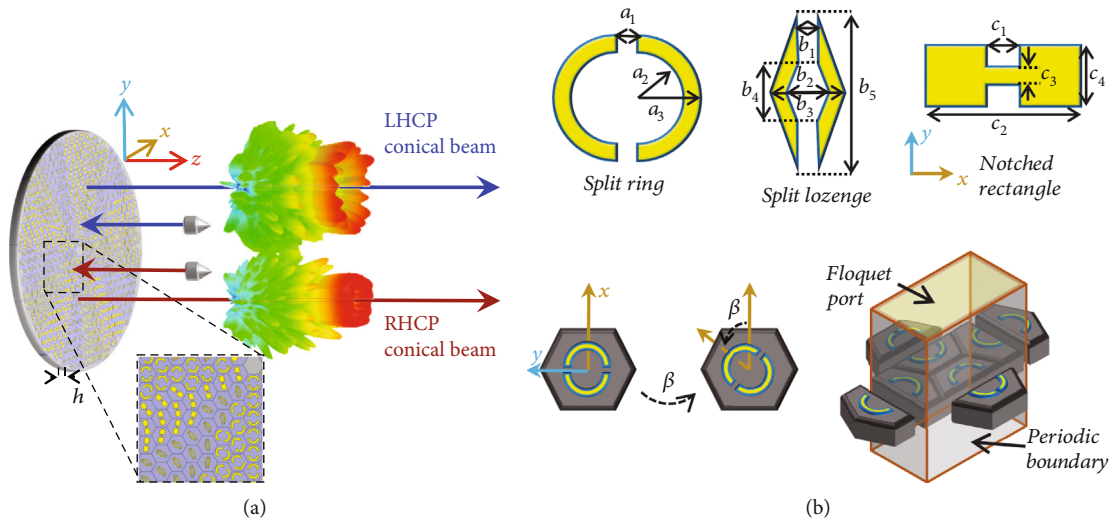

FIGURE 1: (a) Broadband polarization-decoupled metasurface with a zoom-in figure to generate conical beams independently for LHCP and RHCP incidences. (b) Specific metal layer structures of three proposed elements, demonstration of the hexagonal element with an orientation angle of β, and the 3D simulation setup model of the element.

reflective amplitude but attach a 180° phase difference after a 90° self-centered rotation ($\beta = 90\circ$). Therefore, we only need to propose three types of elements, and another three types of elements can be obtained by rotating 90° of original ones. As depicted in Figure 1(b), all these elements are designed to be a single-layer dielectric substrate (F4B, $\varepsilon_r = 2.65$, $h = 3$ mm, and $p = 10$ mm) with a metal ground and a metallic sheet mounted on the two hexagonal surface sides of dielectric substrate. The only difference among elements is the shape of metallic sheets mounted on the upper side of the dielectric substrate shown in Figure 1(b). The designed parameters are $a_1 = 2.5$, $a_2 = 2$, $a_3 = 3$, $b_1 = 1$, $b_2 = 2$, $b_3 = 3$, $b_4 = 3$, $b_5 = 7$, $c_1 = 1.6$, $c_2 = 7.8$, $c_3 = 0.2$, and $c_4 = 2.6$ (unit mm).

Figure 2 shows the characteristics of proposed elements simulated in commercial software high-frequency structural simulator (HFSS) under Floquet port and periodic boundary condition. As presented in Figure 2(a), the magnitude of reflection coefficients for these elements can reach approximately 0.80 or even higher value covering frequencies from 12.5 GHz to 17 GHz with a 30.5% fractional bandwidth. Figure 2(b) depicts the initial phases of proposed elements from 12.5 GHz to 17 GHz, which gives that at any frequency, different elements can cover a 2π phase range together satisfying constraints in (3a). The six initial phase lines in Figure 2(b) show a good parallel characteristic with an almost uniform phase gradient 60° among neighbored lines, satisfying the proposed broadband condition (3b). These evenly distributed initial phase responses could be attributed to the multielement designs, since the obviously different shapes can provide more freedom in designing desired results.

4. A Design Method of Metasurface to Generate Tailored Conical Beams

For metasurface, each element performs as an electromagnetic radiator. According to antenna theory, for a circular metasurface composed of M elements, the far-field radiation pattern with circular polarization can be calculated by [37]

$$E_{\text{rad}}(\mathbf{r}) = \frac{Be^{-jkr}}{4\pi D}\sum_{j}^{M} e^{j\phi(r_j{}')+jkr_j{}'\sin\theta\cos(\varphi_j{}'-\varphi)}, \left(D = \left|\mathbf{r} - \mathbf{r}_j'\right|\right), \tag{5}$$

in which $\mathbf{r}(r, \theta, \varphi)$ is the field's position vector, $\mathbf{r}_j{}'$ $(r_j{}', \varphi_j{}', 0)$ is the position vector of the jth element observing from cylindrical coordinate, k is the wavevector in free space, and B is the inclination factor satisfying $B = jk(1 + \cos\theta)$ derived from the Huygens-Fresnel principle. The phase profile of the jth element $\phi(\mathbf{r}_j{}')$ is

$$\phi\left(\mathbf{r}_j'\right) = \angle e^{jl\varphi_j{}'}, \tag{6}$$

where $\varphi_j{}'$ is the azimuth angle of the jth element $(r_j{}', \varphi_j{}', 0)$ observed from cylindrical coordinate.

Once the arrangement, the period, and the size of metasurface are determined, the far-field radiation pattern and the cone angle θ_m, the angle of θ with maximum far-field radiation energy, can be calculated based on (5) and (6). The triangular arrangement is applied in our metasurface since it has better isotropy [38]. The period p of element is 10 mm. Based on (5) and (6) calculated with different metasurface sizes, we uncover the relationship among cone angle θ_m, OAM mode $|l|$, and the size of metasurface depicted in Figure 3(a), in which the cone angle increases with the increasing of OAM mode under a certain size of metasurface, while it decreases with the increasing of radius under a specific OAM mode. The quantitative relationship in Figure 3(a) is essential to tailor conical beams featuring expected cone angles or OAM modes. The OAM beam will be poor if the size of metasurface is too small, so we force

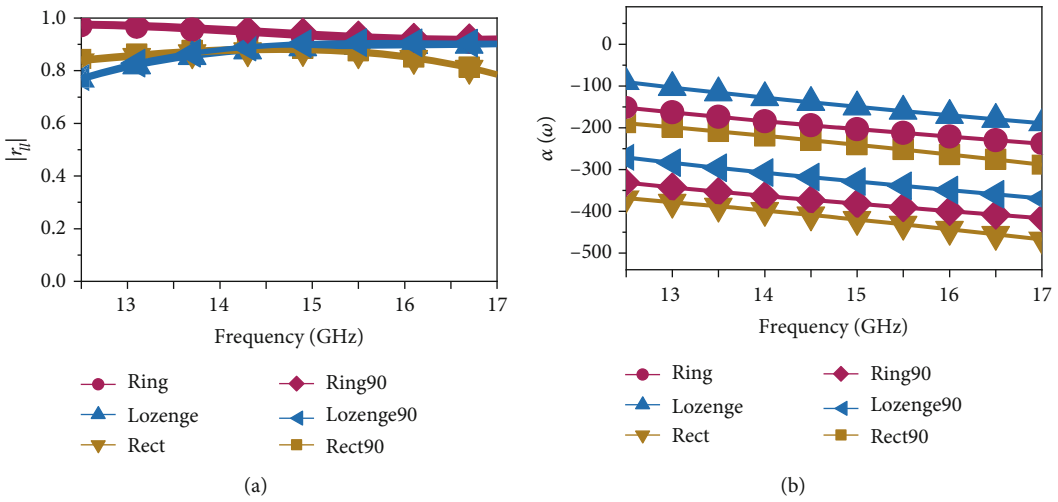

FIGURE 2: (a) Magnitude of reflection coefficients of the six elements. (b) Initial phase distribution of the six elements.

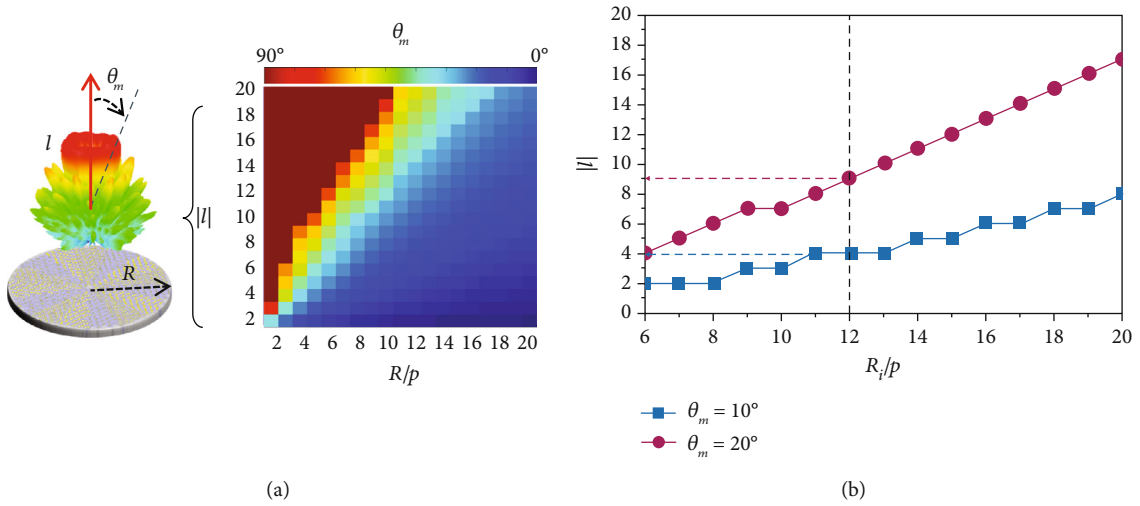

FIGURE 3: (a) Relationship among conical beam cone angle, OAM mode, and metasurface size. (b) Relationship between the size of metasurface and the conical beam OAM mode when the expected cone angles are 10° and 20°.

$\theta_m = 90\circ$ when the results of θ_m in Figure 3(a) become inaccurate for small R/p.

Based on previous discussions, a metasurface can be designed as follows. First, the desired phase profiles ϕ_{ll} and ϕ_{rr} (for LHCP and RHCP) should be determined according to the expected cone angle θ_m in Figure 3(a). Then, for every element, it should be arranged according to phase profile $(\phi_{rr} + \phi_{ll})/2$ and rotate a specific angle according to phase profile $(\phi_{rr} - \phi_{ll})/4$. For example, we aim to generate conical beams for LHCP and RHCP with cone angles 10° and 20°, respectively. According to Figure 3(a), to generate conical beams with angles 10° and 20°, the relationship between OAM mode and the size of metasurface is extracted to Figure 3(b). Normally, the size of metasurface is determined by needs. In this example, the size of the designed metasurface is 12 times of the element period ($R/p = 12$), so referring to dash lines in Figure 3(b), the corresponding OAM mode is ±4 when the expected cone angle is 10° for LHCP and the OAM mode is ±9 when the expected cone angle is 20° for RHCP. Following the fabricating procedure, the desired phase responses ϕ_{ll} (for LHCP, $l = 4$) and ϕ_{rr} (for RHCP, $l = -9$) are firstly depicted in Figure 4. Then, phase profiles of $(\phi_{rr} - \phi_{ll})/4$ and $(\phi_{rr} + \phi_{ll})/2$ are illustrated in Figure 4. Finally, the proposed elements are arranged and rotated in accordance with the given phase profiles to compose the metasurface depicted in Figure 4. Once the phase profile is determined, the theoretical far-field radiation patterns at 15 GHz can be calculated by (4a), (4b), and (5), which are revealed in Figure 5. For both LHCP and RHCP cases, the maximum energy of the reflected beams covers a circumferential range from 0° to 360° at cone angles 10° and 20°, respectively, which demonstrates that the designed phase profiles can generate conical beams with tailored cone angles.

5. Simulation and Experiment

In this part, the proposed metasurface in Figure 4 is simulated in HFSS. The reflected fields are obtained under LHCP

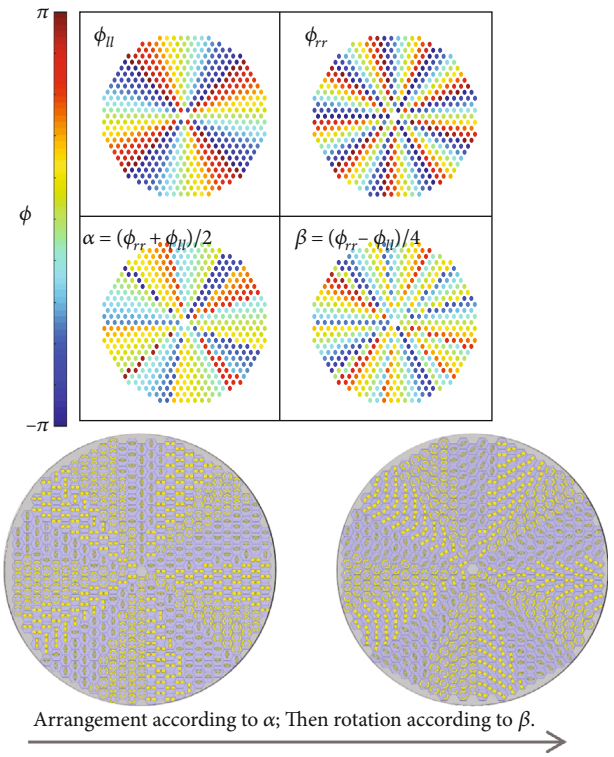

FIGURE 4: Phase profiles and the designing procedure of metasurface: elements are arranged according to $\alpha = (\phi_{rr} + \phi_{ll})/2$ and are then rotated according to $\beta = (\phi_{rr} - \phi_{ll})/4$.

and RHCP plane wave excitations at 15 GHz. Regarding to copolarized $|E|$-field patterns in Figure 5, for both LHCP and RHCP excitations, the maximum energy has covered 360° in the azimuth plane at exactly 10° and 20°, respectively. The number of 2π phase-changing spirals along dash lines denoted on phase pattern ($\angle E$) in Figure 5 shows that the OAM mode is 4 for LHCP and -9 for RHCP. These simulated results conform with the theoretical results, which can verify the effectiveness of the proposed theories. Moreover, as depicted in Figure 5, the cross-polarization patterns for both LHCP and RHCP excitations are low enough, which is significant for the metasurface to reach a high conversion efficiency, η.

$$\eta = \frac{\iint_s |E_{\text{co-pol}}|^2 ds}{\iint_s |E_{\text{co-pol}}|^2 ds + \iint_s |E_{\text{cross-pol}}|^2 ds}, \tag{7}$$

in which s is the area of upper space. In this case, the proposed metasurface can obtain a high enough η (with 77.6% for LHCP and 76% for RHCP, respectively).

To verify the broadband (from 12.5 GHz to 17 GHz) characteristic of the proposed metasurface, copolarized far-field radiation patterns at *xoz*-plane and *yoz*-plane produced by (4a) and (4b) and HFSS simulations are compared at 13 GHz, 15 GHz, and 17 GHz. Figure 6(a) is the far-field patterns under LHCP excitation. The conical-shaped pattern could be found at both *xoz*- and *yoz*-planes with cone angle $\theta_m \approx 10\circ$. Figure 6(b) shows the far-field patterns under the

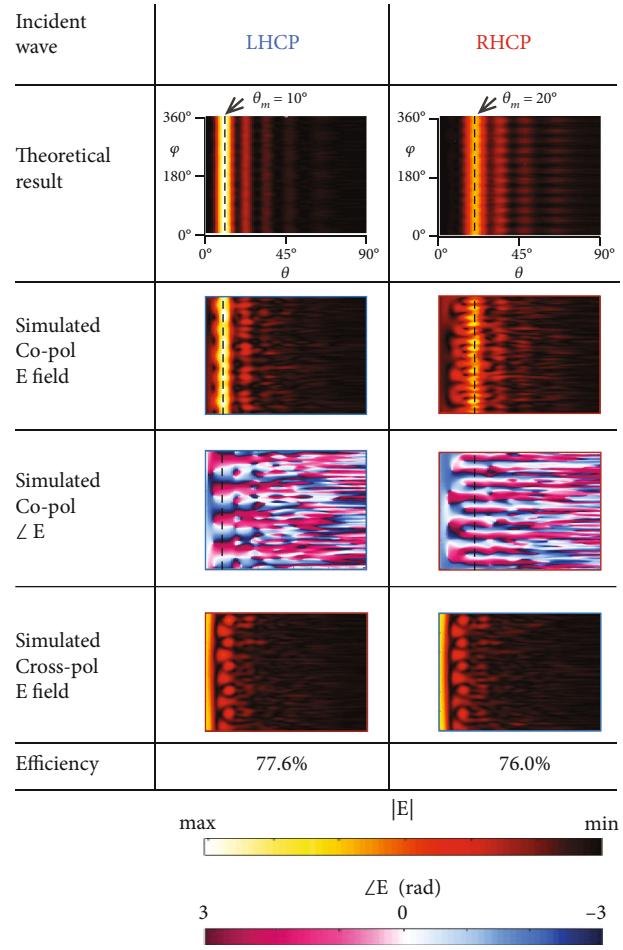

FIGURE 5: Theoretical and simulated results of far-field patterns for conical beams with RHCP and LHCP excitations on the proposed metasurface.

excitation of RHCP wave, where broadband conical beams are generated. The cone angles are strictly consistent with the expected values at designed frequency (15 GHz). Although cone angles are not a strictly fixed value within the desired bandwidth due to the frequency dependence, an intrinsic characteristic, of the OAM pattern, the generated radiation patterns also show a conical-shaped beam with near -10 dB side lobes and can be accurately predicted by theoretical results.

To verify the proposed metasurface experimentally, we build a specific experiment setup to generate the aforementioned conical beams. Figure 7 shows the front and side views of the experiment setup, where the metasurface is placed at a 3D-printed stand and two Archimedes spiral antennas are located at the position vector $\mathbf{r}_f = [0, 0, 200]$ and $\mathbf{r}_f = [0, -120, 200]$ on the stand referring to the center of metasurface (unit mm). The upper antenna is a right-hand spiral antenna, which is normal to the metasurface, and the lower antenna is a left-hand spiral antenna which is oriented to the center of the metasurface. In this case, additional compensated phases should be imparted into each element to compensate the sphere waves nonideally

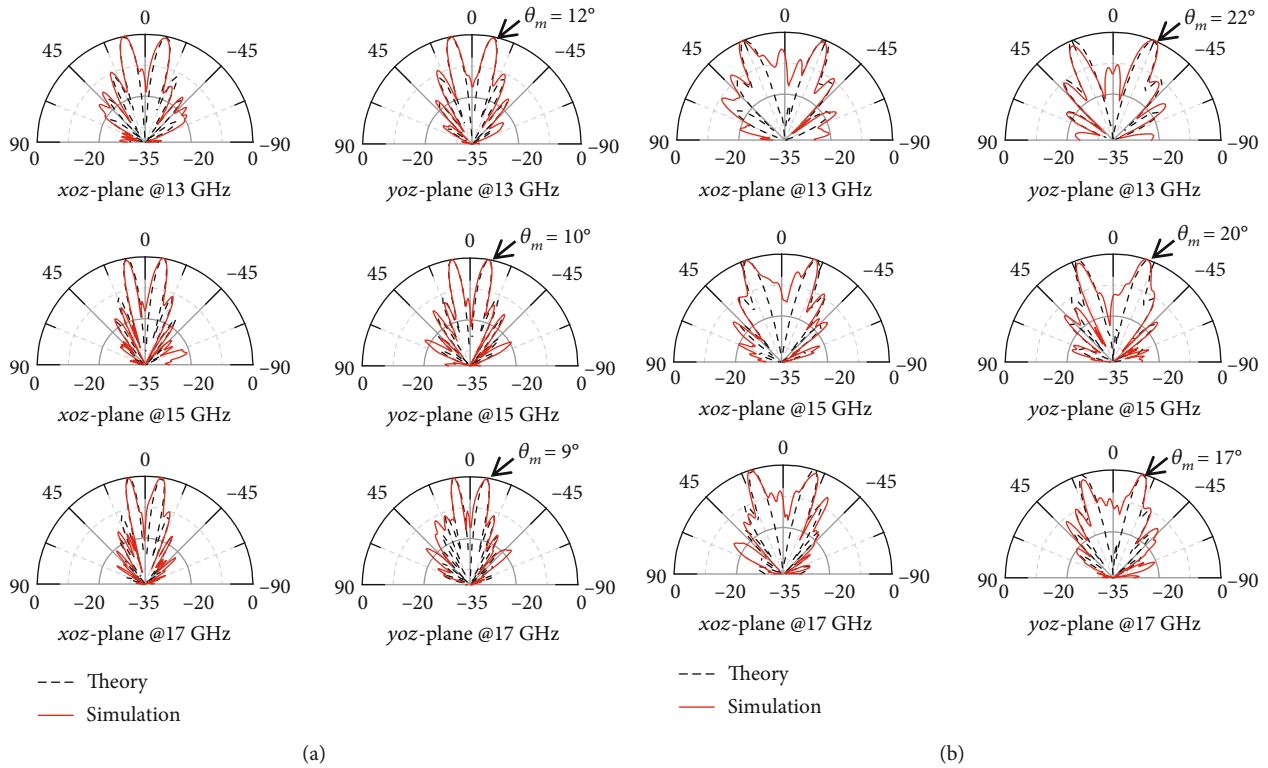

FIGURE 6: Comparison of theoretical and simulated results of far-field radiation patterns at *xoz*-plane and *yoz*-plane under the excitation of (a) LHCP and (b) RHCP.

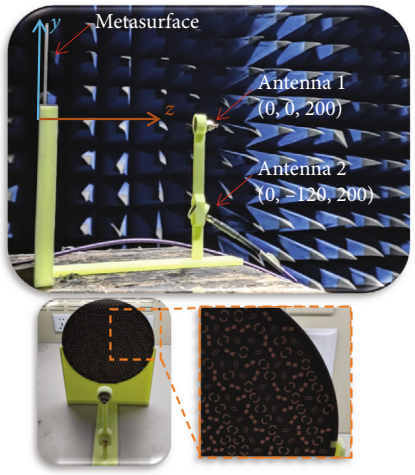

FIGURE 7: Side and front views of the manufactured metasurface and the feeding antennas and a close-up picture of fabricated metasurface.

generated by these two implemented antennas. For the *j*th element in the metasurface, the compensated phase ϕ^c could be obtained by [39]

$$\phi^c = k_0 \left| \mathbf{r}_j{}' - \mathbf{r}_f \right|, \tag{8}$$

in which k_0 is the propagation constant, $\mathbf{r}_j{}'$ is the position vector of the *j*th element, and $\boldsymbol{r}_{\mathrm{f}}$ is the position vector of the antenna. Therefore, phase responses used to design the fabricated metasurface are

$$\phi_{ll} = \phi_{ll}^{l} + \phi_{ll}^{c}, \tag{9a}$$

$$\phi_{rr} = \phi_{rr}^{l} + \phi_{rr}^{c}. \tag{9b}$$

The far-field radiation patterns of both simulated and measured results under the excitations of LHCP and RHCP spiral antennas at 13 GHz, 15 GHz, and 17 GHz are shown in Figure 8. Although the far-field patterns are not as symmetric as those with plane wave incidences in Figure 6 due to the nonideal excitation and the offset design, the copolarized measuring results at 15 GHz in Figures 8(a) and 8(b) can still show the expected conical beams with near -9 dB side lobes and fit the simulated results at both *xoz*-plane and *yoz* -plane. For both RHCP and LHCP excitations, the magnitude of cross-polarized patterns is almost -6 dB lower than that of the corresponding copolarization patterns, which verifies the high efficiency of the proposed metasurface. For broadband performance, experiments are conducted at 13 GHz and 17 GHz with the results presented in Figure 8(c), in which conical beams can be found in copolarized far-field patterns under LHCP and RHCP excitations. The experiment results confirm that we can generate broadband cone angle-tailored conical beams with LHCP and RHCP waves using the proposed metasurface. Moreover, better experiment results could be achieved if a broadband dual-polarization antenna with high performance was used

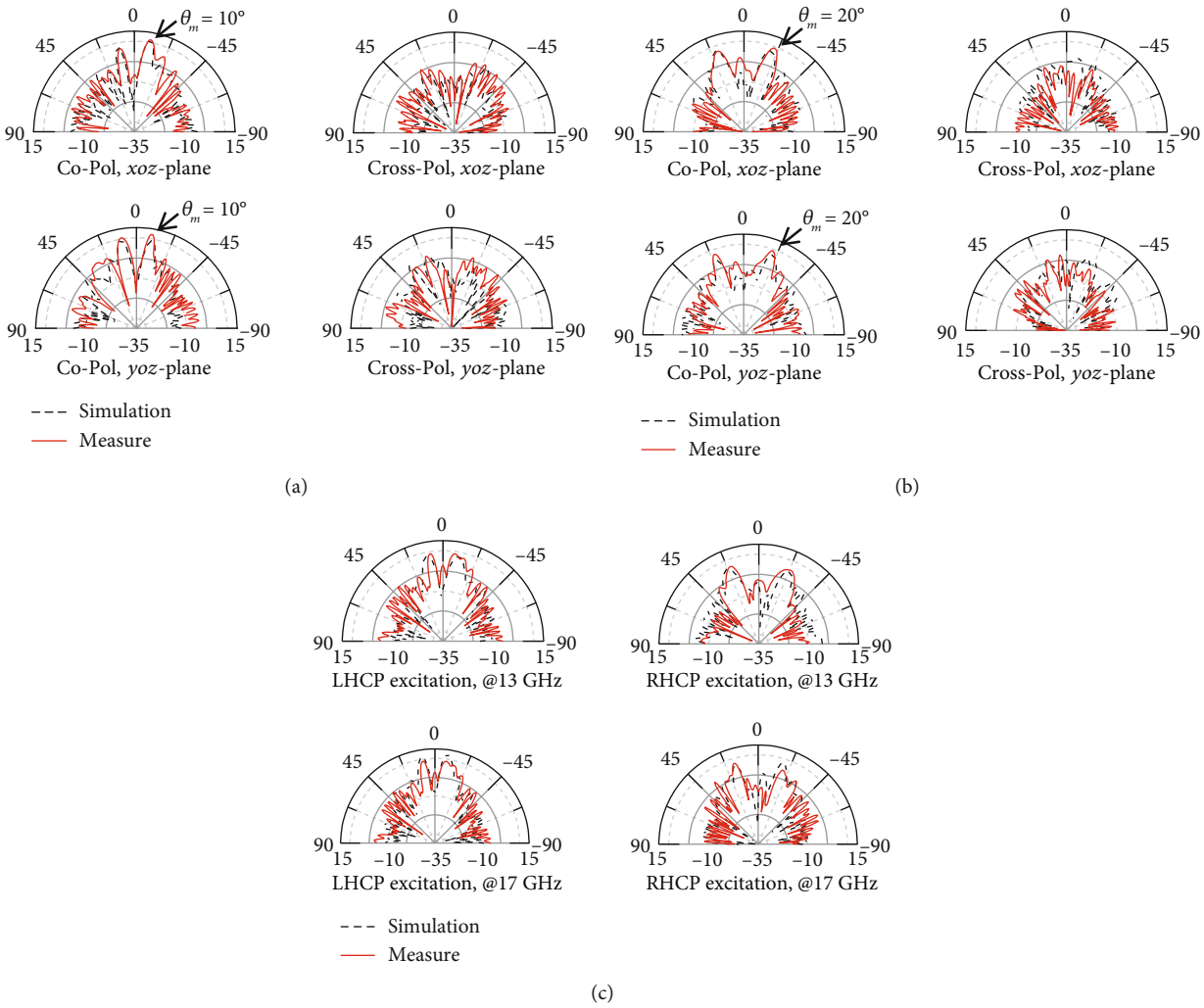

Figure 8: Comparison between simulated results and the experimental results of far-field radiation patterns under (a) LHCP excitation and (b) RHCP excitation at 15 GHz and (c) both LHCP and RHCP excitations at 13 GHz and 17 GHz.

and placed normal to metasurface rather than applying two antennas requiring offset feed in our experiment.

6. Conclusion

In this work, we have proposed a metasurface to independently generate cone angle-tailored OAM conical beams with both LHCP and RHCP. The designed metasurface has been verified in theorem, simulation, and physical experiments resulting in reasonable conformity with expectations. The cone angle of generated conical beams can be tailored independently with LHCP and RHCP excitations from 12.5 GHz to 17 GHz covering a broad bandwidth. Compared with traditional conical beams, we can achieve dual-polarized conical beams with LHCP and RHCP excitations. In particular, we propose three types of elements, which can provide more degree of freedom in dual-polarization decoupling and broadband design. In addition, depending on the found relationship among cone angle, OAM mode, and the size of metasurface, the generated conical beams or OAM modes are tailorable, which can be expanded to the applications of beam steering and tailored OAM beams. Although we conducted the experiment at 12.5 GHz to 17 GHz, the broadband theory of polarization-decoupled elements and the design process are also suitable in terahertz and optical fields.

Data Availability

No underlying data was collected or produced in this study.

Conflicts of Interest

The authors declare that they have no conflicts of interest.

Acknowledgments

This work was supported in part by the National Natural Science Foundation of China under Grants 61721001 and 61971115.

References

[1] L. Cui, S.-S. Qi, W. Wu, and D.-G. Fang, "High gain conical beam antenna array exploiting grating lobes," *IEEE Transactions on Antennas and Propagation*, vol. 63, no. 2, pp. 848–853, 2015.

[2] W. H. Chen, J. W. Sun, X. Wang et al., "A novel planar switched parasitic array antenna with steered conical pattern," *IEEE Transactions on Antennas and Propagation*, vol. 55, no. 6, pp. 1883–1887, 2007.

[3] J. Sun, K. Chen, K. Qu, J. Zhao, T. Jiang, and Y. Feng, "Controlling conical beam carrying orbital angular momentum with transmissive metasurface," *International Journal of Antennas and Propagation*, vol. 2021, Article ID 9951644, 10 pages, 2021.

[4] K. L. Lau and K. M. Luk, "A wideband circularly polarized conical-beam patch antenna," *IEEE Transactions on Antennas and Propagation*, vol. 54, no. 5, pp. 1591–1594, 2006.

[5] G. Ding, K. Chen, T. Jiang, B. Sima, J. Zhao, and Y. Feng, "Full control of conical beam carrying orbital angular momentum by reflective metasurface," *Optics Express*, vol. 26, no. 16, pp. 20990–21002, 2018.

[6] Y. Bao, J. Ni, and C.-W. Qiu, "A minimalist single-layer metasurface for arbitrary and full control of vector vortex beams," *Advanced Materials*, vol. 32, no. 6, article 1905659, 2020.

[7] P. Li, Y. Zhang, S. Liu et al., "Generation of perfect vectorial vortex beams," *Advanced Materials*, vol. 41, no. 10, pp. 2205–2208, 2016.

[8] R. A. Herring, "A new twist for electron beams," *Science*, vol. 331, no. 6014, pp. 155-156, 2011.

[9] K. Liu, Y. Cheng, Y. Gao, X. Li, Y. Qin, and H. Wang, "Superresolution radar imaging based on experimental OAM beams," *Applied Physics Letters*, vol. 110, no. 16, article 164102, 2017.

[10] Y. Yan, G. Xie, M. P. J. Lavery et al., "High-capacity millimetre-wave communications with orbital angular momentum multiplexing," *Nature Communications*, vol. 5, no. 1, p. 4876, 2014.

[11] N. Bozinovic, Y. Yue, Y. Ren et al., "Terabit-scale orbital angular momentum mode division multiplexing in fibers," *Science*, vol. 340, no. 6140, pp. 1545–1548, 2013.

[12] M. Lin, Y. Gao, P. Liu, and J. Liu, "Theoretical analyses and design of circular array to generate orbital angular momentum," *IEEE Transactions on Antennas and Propagation*, vol. 65, no. 7, pp. 3510–3519, 2017.

[13] L. Kang, H. Li, J. Zhou, S. Zheng, and S. Gao, "A mode-reconfigurable orbital angular momentum antenna with simplified feeding scheme," *IEEE Transactions on Antennas and Propagation*, vol. 67, no. 7, pp. 4866–4871, 2019.

[14] P. Genevet, J. Lin, M. A. Kats, and F. Capasso, "Holographic detection of the orbital angular momentum of light with plasmonic photodiodes," *Nature Communications*, vol. 3, no. 1, p. 1278, 2012.

[15] J. J. Chen, Q. N. Lu, F. F. Dong, J. J. Yang, and M. Huang, "Wireless OAM transmission system based on elliptical microstrip patch antenna," *Optics Express*, vol. 24, no. 11, pp. 11531–11538, 2016.

[16] Y. Chen, S. Zheng, Y. Li et al., "A flat-lensed spiral phase plate based on phase-shifting surface for generation of millimeter-wave OAM beam," *IEEE Antennas and Wireless Propagation Letters*, vol. 15, pp. 1156–1158, 2016.

[17] N. Yu, P. Genevet, M. A. Kats et al., "Light propagation with phase discontinuities: generalized laws of reflection and refraction," *Science*, vol. 334, no. 6054, pp. 333–337, 2011.

[18] S. Sun, Q. He, S. Xiao, Q. Xu, X. Li, and L. Zhou, "Gradient-index meta-surfaces as a bridge linking propagating waves and surface waves," *Nature Materials*, vol. 11, no. 5, pp. 426–431, 2012.

[19] X. G. Zhang, W. X. Jiang, H. L. Jiang et al., "An optically driven digital metasurface for programming electromagnetic functions," *Nature Electronics*, vol. 3, no. 3, pp. 165–171, 2020.

[20] M. L. N. Chen, L. J. Jiang, and W. E. I. Sha, "Ultrathin complementary metasurface for orbital angular momentum generation at microwave frequencies," *IEEE Transactions on Antennas and Propagation*, vol. 65, no. 1, pp. 396–400, 2017.

[21] K. Zhang, Y. Yuan, D. Zhang et al., "Phase-engineered metalenses to generate converging and non-diffractive vortex beam carrying orbital angular momentum in microwave region," *Optics Express*, vol. 26, no. 2, pp. 1351–1360, 2018.

[22] H. Sroor, Y.-W. Huang, B. Sephton et al., "High-purity orbital angular momentum states from a visible metasurface laser," *Nature Photonics*, vol. 14, no. 8, pp. 498–503, 2020.

[23] Z. Akram, X. Li, Z. Qi et al., "Broadband high-order OAM reflective metasurface with high mode purity using subwavelength element and circular aperture," *IEEE Access*, vol. 7, pp. 71963–71971, 2019.

[24] L.-J. Yang, S. Sun, and W. E. I. Sha, "Ultrawideband reflection-type metasurface for generating integer and fractional orbital angular momentum," *IEEE Transactions on Antennas and Propagation*, vol. 68, no. 3, pp. 2166–2175, 2020.

[25] W. Luo, S. Sun, H.-X. Xu, Q. He, and L. Zhou, "Transmissive ultrathin pancharatnam-berry metasurfaces with nearly 100% efficiency," *Physical Review Applied*, vol. 7, no. 4, article 044033, 2017.

[26] M. Jia, Z. Wang, H. Li et al., "Efficient manipulations of circularly polarized terahertz waves with transmissive metasurfaces," *Light: Science & Applications*, vol. 8, no. 1, p. 16, 2019.

[27] H. Xu, G. Hu, M. Jiang et al., "Wavevector and frequency multiplexing performed by a spin-decoupled multichannel metasurface," *Advanced Materials Technologies*, vol. 5, no. 1, article 1900710, 2020.

[28] W.-L. Guo, G.-M. Wang, W.-Y. Ji, Y.-L. Zheng, K. Chen, and Y. Feng, "Broadband spin-decoupled metasurface for dual-circularly polarized reflector antenna design," *IEEE Transactions on Antennas and Propagation*, vol. 68, no. 5, pp. 3534–3543, 2020.

[29] Z. X. Wang, J. W. Wu, L. W. Wu et al., "High efficiency polarization-encoded holograms with ultrathin bilayer spin-decoupled information metasurfaces," *Advanced Optical Materials*, vol. 9, no. 5, article 2001609, 2021.

[30] R. C. Devlin, A. Ambrosio, N. A. Rubin, J. P. B. Mueller, and F. Capasso, "Arbitrary spin-to-orbital angular momentum conversion of light," *Science*, vol. 358, no. 6365, pp. 896–901, 2017.

[31] G. Ding, K. Chen, X. Luo, J. Zhao, T. Jiang, and Y. Feng, "Dual-helicity decoupled coding metasurface for independent spin-to-orbital angular momentum conversion," *Physical Review Applied*, vol. 11, no. 4, article 044043, 2019.

[32] Y.-W. Huang, N. Rubin, A. Ambrosio, Z. Shi, C.-W. Qiu, and E. Capasso, "Versatile total angular momentum generation using cascaded J-plates," *Optics Express*, vol. 27, no. 5, pp. 7469–7484, 2019.

[33] K. Qu, K. Chen, Q. Hu, J. Zhao, T. Jiang, and Y. Feng, "Deep-learning-assisted inverse design of dual-spin/frequency metasurface for quad-channel off-axis vortices multiplexing," *Advanced Photonics Nexus*, vol. 2, no. 1, 2023.

[34] L. Yang, S. Sun, W. E. I. Sha, and J. Hu, "Bifunctional integration performed by a broadband high-efficiency spin-decoupled metasurface," *Advanced Optical Materials*, vol. 11, no. 2, article 2201955, 2023.

[35] J.-J. Sun, S. Sun, and L.-J. Yang, "Machine learning-based fast integer and fractional vortex modes recognition of partially occluded vortex beams," *IEEE Transactions on Antennas and Propagation*, vol. 70, no. 8, pp. 6775–6784, 2022.

[36] C. Menzel, C. Rockstuhl, and F. Lederer, "Advanced Jones calculus for the classification of periodic metamaterials," *Physical Review A*, vol. 82, no. 5, article 053811, 2010.

[37] S. Jiang, C. Chen, J. Ding, H. Zhang, and W. Chen, "Alleviating orbital-angular-momentum-mode dispersion using a reflective metasurface," *Physical Review Applied*, vol. 13, no. 5, article 054037, 2020.

[38] L.-J. Yang, S. Sun, and W. E. I. Sha, "Manipulation of orbital angular momentum spectrum using shape-tailored metasurfaces," *Advanced Optical Materials*, vol. 9, no. 2, article 2001711, 2021.

[39] L.-J. Yang, S. Sun, W. E. I. Sha, Z. Huang, and J. Hu, "Arbitrary vortex beam synthesis with donut-shaped metasurface," *IEEE Transactions on Antennas and Propagation*, vol. 70, no. 1, pp. 573–584, 2022.